DSC-Vol. 58, Proceedings of the ASME Dynamics Systems
and Control Division
ASME 1996

PREVIEW CONTROL OF A SUPERCONDUCTING MAGLEV VEHICLE

Mark L. Nagurka and Ssu-Kuei Wang

Carnegie Mellon Research Institute
700 Technology Drive, P.O. Box 2950
Pittsburgh, PA 15230-2950

ABSTRACT

A dynamic model of a magnetically-levitated (maglev) vehicle negotiating an elevated guideway is presented. The vehicle employs an electromagnetic suspension (EMS) system with canted magnets that provide simultaneous levitation and guidance. The modeling effort is focused on deriving a realistic dynamic model that includes a five degree-of-freedom nonlinear vehicle model, a superconducting magnet model, and a simply supported, multi-spanned guideway model. The maglev vehicle/guideway model is the basis for testing a proposed control strategy consisting of linear quadratic (LQ) optimal control with a preview (feedforward) feature. The LQ optimal control is augmented with integral action to avoid steady-state gap errors which might otherwise arise from guideway offsets. Simulation studies explore the effectiveness of the controller. The results reveal that the magnet module input voltages and gap errors decrease as the preview distance increases. However, the vehicle performance is limited due to a tradeoff between the carbody acceleration and the gap error.

1 INTRODUCTION

A primary safety requirement for maglev dynamic performance is the ability to operate over a wide range of conditions without leaving or contacting the guideway (in analogy to derailment of rail vehicles). In maglev systems that rely on electromagnetic suspension (EMS) forces, this requirement is accomplished via active feedback control (Heinrich and Kretzschmar, 1989). The control system plays multiple roles, one of which is to ensure overall safe performance by actively positioning the vehicle relative to the guideway. The aim is to maintain a nominal air gap for both vertical lift and lateral guidance. The controller also tunes the suspension impedance to attain acceptable ride quality.

Previous work has explored the use of conventional linear quadratic (LQ) optimal control to stabilize an EMS maglev system and regulate the air gap (Kortüm and Utzt, 1984). A difficulty is that a nonzero steady-state gap error can result from a constant disturbance, such as a step guideway offset. This problem can be circumvented by using an optimal integral control technique (Anderson and Moore, 1990), in which integrators are inserted in the controller to eliminate steady-state errors due to constant disturbances. Furthermore, if information about the disturbance input is known *a priori*, it can be used by an extended LQ optimal controller, called an optimal preview controller (Bender, 1968; Tomizuka, 1976). With the advent of modern microcomputer technology, optimal preview control is implementable. It has been proposed and studied for automotive applications (Hać, 1992; Louam, *et al.*, 1992; Peng and Tomizuka, 1993; Langlois and Anderson, 1995) where promising results have been shown, but it has not been reported in maglev vehicle designs.

In this paper LQ optimal control with integral action and preview is proposed for a maglev system. As noted, the integral action ensures zero steady-state gap error due to step disturbances. The preview control uses guideway information in front of the vehicle to improve overall dynamic performance. The preview controller is combined with a detailed maglev/guideway model to form a complete nonlinear simulation model. The maglev vehicle in this study is based on Grumman's system concept (Proise, *et al.*, 1993) which uses a superconducting (SC) electromagnetic suspension (EMS) system. Combined lift and guidance is achieved by attractive forces using a single set of inclined magnets on both sides of the vehicle. Simulation results of this model under the influence of guideway flexibility and guideway irregularities are reported, where performance is measured in terms of gap error for safety, vehicle vertical and lateral accelerations for ride comfort, and magnet input voltage for energy cost.

2 SYSTEM MODEL DERIVATIONS

2.1 Vehicle Model

An inertial coordinate frame ($X_I Y_I Z_I$) is assumed to move along the guideway longitudinal direction at a constant vehicle speed, V_v. The

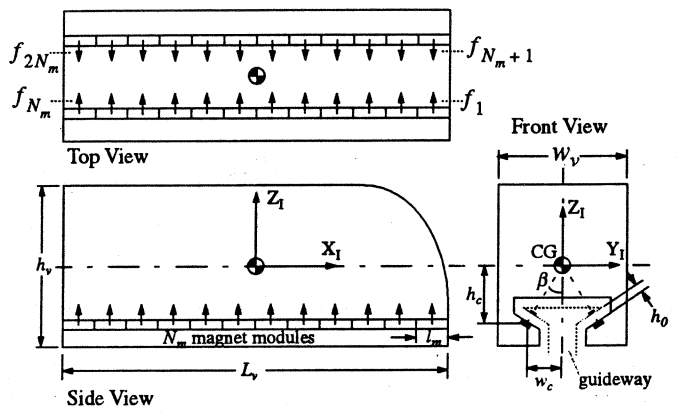

Figure 1 Vehicle Configuration

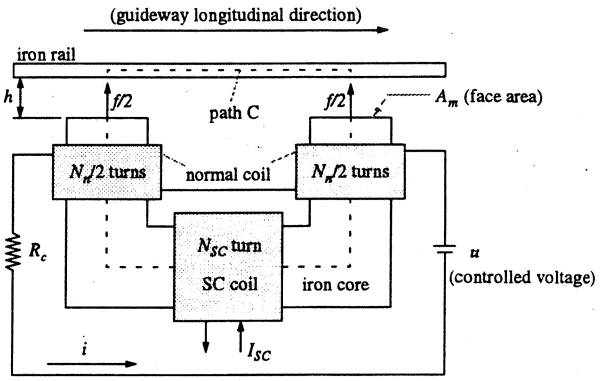

Figure 2 Single SC Magnet

vehicle motion is characterized by the lateral, y_c, and vertical, z_c, displacements of the carbody CG, and the roll, ψ_c, pitch, θ_c, and yaw, ϕ_c, angles of a carbody coordinate frame ($X_C Y_C Z_C$).

Figure 1 shows the vehicle configuration in its nominal position. There are an even number, N_m, of magnet modules on each side inclined at angle β from vertical. At this angle the magnetic forces (attracted to iron rails fixed in the guideway) pass through the longitudinal axis of the vehicle when the vehicle is in its nominal position. The magnetic force from each magnet module (containing a set of magnets controlled as a group) is assumed to be distributed uniformly along the module length, l_m. The vehicle length and height are denoted by L_v and h_v, respectively. Also shown in the figure are the nominal air gap, h_0, and the height and width between the module and the carbody CG, denoted by h_c and w_c, respectively.

The derivation of the equations of motion consists of three steps: (*i*) identification of the air gap at each module, (*ii*) determination of the resultant magnetic force and corresponding moment, and (*iii*) application of Newton's second law and Euler's equation. The resulting equations of motion for the vehicle model can be written as

$$F_y = M_v \ddot{y}_c \ , \ F_z - M_v g = M_v \ddot{z}_c \qquad (1),(2)$$

$$M_x = I_x \dot{\omega}_x - (I_y - I_z)\omega_y \omega_z \ , \ M_y = I_y \dot{\omega}_y - (I_z - I_x)\omega_z \omega_x \qquad (3),(4)$$

$$M_z = I_z \dot{\omega}_z - (I_x - I_y)\omega_x \omega_y \ , \ \dot{\phi}_c = \omega_x + (\omega_y \sin\phi_c + \omega_z \cos\phi_c)\tan\theta_c \qquad (5),(6)$$

$$\dot{\theta}_c = \omega_y \cos\phi_c - \omega_z \sin\phi_c \ , \ \dot{\psi}_c = (\omega_y \sin\phi_c + \omega_z \cos\phi_c)/\cos\theta_c \qquad (7),(8)$$

where g is the acceleration due to gravity, and ω_x, ω_y, and ω_z are the roll, pitch, and yaw angular velocities, respectively, in the carbody coordinate frame. In Eqs. (1) and (2) F_y and F_z are the resultant force components in the initial Y_I and Z_I directions, respectively. There is no equation of motion in the longitudinal direction since constant vehicle speed is assumed. In Eqs. (3)-(5) M_x, M_y, and M_z are the resultant moment components in the carbody X_C, Y_C, and Z_C directions, respectively. The directions of the resultant force and moment depend on the motion of the carbody relative to the guideway while the magnitude of the resultant force is specified by the controller. The vehicle equations of motion can be represented equivalently by ten first-order ordinary differential equations (ODEs). The full derivation appears in (Wang, 1995).

2.2 SC Magnet Model

A single SC magnet, shown schematically in Fig. 2, consists of an iron-core magnet, a SC coil wrapped on the back leg of the iron core, and a set of serially connected normal coils attached to both pole ends of the iron core. N_{SC} and N_n are the number of turns in the SC coil and the normal coils, respectively. The current in the SC coil is I_{SC}. The trim current, i, in the normal coils is driven by a controlled voltage, u, to maintain the air gap, h, at its nominal value. The resistance of the normal coil is denoted by R_c and the face area of each magnetic pole is denoted by A_m.

In Fig. 2, the magnet is attracted to the guideway iron rail by attractive force, f, set up by the magnetic flux density, B_m, in the air gap, *i.e.*,

$$f = \frac{B_m^2 A_m}{\mu_0} \ , \ B_m = \frac{\mu_0}{2h}(N_{SC} I_{SC} + N_n i) \qquad (9),(10)$$

where μ_0 denotes the permeability of air. In Eq. (9), f can be derived using the law of conservation of energy for the magnetic energy stored in the air gap (*e.g.*, Iskander, 1992). In Eq. (10), B_m can be obtained by applying Ampere's law along path C in Fig. 2. Also, it is assumed that the leakage flux in the iron rail and iron core is negligible and the air gap is sufficiently narrow such that the total flux in the iron core flows across the gap without loss.

The SC current, I_{SC}, provides lifting capability to compensate for the vehicle weight and is assumed constant in this study. The trim current, i, is achieved by a power supply with controlled voltage, u. From Kirchhoff's voltage law, the relation between the trim current and the controlled voltage, u, is

$$u - R_c i - N_n \frac{d(B_m A_m)}{dt} = 0 \qquad (11)$$

In Eq. (11), the last term on the left-hand side is the electromotive force (*emf*) induced by the normal coil. (The *emf* induced by the SC coil is

absent since constant SC current is assumed.)

Each magnet module houses n_m SC magnets. Since it is assumed that the magnetic force of each magnet in a module is generated by the same power supply, the total magnetic force is n_m times the force set up by a single magnet. Thus, the magnetic force at a module can be written as

$$f_j = \frac{\mu_0 A_m n_m}{4h_j^2}(N_{SC}I_{SC}+N_n i_j)^2 \tag{12}$$

for module $j=1,...,2N_m$, where h_j is the air gap at the j-th module and the trim current, i_j, is determined from Eq. (11) as

$$u_j = R_c i_j + \frac{\mu_0 A_m N_n^2}{2h_j}\frac{di_j}{dt} - \frac{\mu_0 A_m N_n (N_{SC}I_{SC}+N_n i_j)}{2h_j^2}\frac{dh_j}{dt} \tag{13}$$

for $j=1,...,2N_m$, with u_j being the controlled voltage for the j-th module.

In summary, the dynamics of the SC magnet model are described by Eq. (13) for each module and can be represented by $2N_m$ first-order ODEs. The resulting trim current and the constant SC current in each magnet module produce a magnetic flux which sets up the attractive magnetic force between the iron core and the iron rail. The magnetic force at each module, described by Eq. (12), is a nonlinear function of the trim current, SC current, and air gap.

2.3 Guideway Model

An elevated, multi-spanned, tangent guideway model is assumed, with each span modeled by a Bernoulli-Euler beam with simply supported ends. The equation of motion for a single span can be expressed as

$$EI\frac{\partial^4}{\partial x_s^4}\tilde{w}_s(x_s,t)+c\frac{\partial}{\partial t}\tilde{w}_s(x_s,t)+\gamma\frac{\partial^2}{\partial t^2}\tilde{w}_s(x_s,t)=\tilde{f}(x_s,t) \tag{14}$$

where x_s is the span axial coordinate, EI is the bending rigidity, c is the viscous damping coefficient, γ is the span mass per unit length, $\tilde{w}_s(x_s,t)$ is the span vertical deflection, and $\tilde{f}(x_s,t)$ is the loading force per unit length due to the moving vehicle. (The use of the superscript ~ denotes functional dependence on both space and time.)

The process for deriving the vehicle/guideway interaction involves three steps. The first step is to convert the magnetic forces of the modules into the distributed loading forces on the spans. The second step is to solve for the distributed span deflections using a modal analysis method in which the span deflections are expressed using n_s mode shapes and modal amplitudes. The final step is to obtain the guideway deflection observed at each module.

In these steps, the vehicle/guideway interaction is considered in the time interval $[t_0, t_f]$. At $t=t_0$, the vehicle is completely located on a first span with its nose just about to enter a second span. As time increases, the vehicle excites the first span and then both spans simultaneously. In this study, it is assumed that the vehicle length, L_v, is less than the guideway span length, L_s. As a result, the vehicle is completely located on the second span at $t=t_f$. For multi-span configurations, additional spans are "daisy-chained", *i.e.*, at $t=t_f$, the clock is reset to $t=t_0$ and the algorithm for the following span is re-applied (Cherchas, 1979). Explicit equations for these cases can be found in (Wang, 1995).

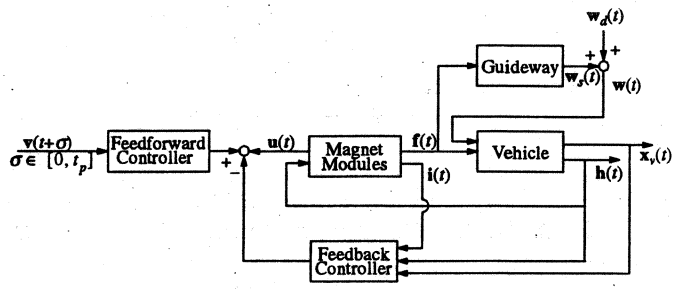

Figure 3 Block Diagram of Complete Maglev System

In summary, the input to the guideway model is the magnetic force at each magnet module and the output is the corresponding guideway deflection. The guideway dynamic analysis considers the first n_s modes of beam vibration. The guideway model accounts for two sequential spans (which are concatenated for guideways involving more spans). Since each span requires n_s second-order ODEs, the governing equations consist of $2n_s$ second-order ODEs for two spans.

2.4 Combined Maglev Model

The block diagram of Fig. 3 depicts the interaction among the dynamic models for the vehicle, magnet modules, and guideway. The controlled variables are the applied voltages u_j ($j=1,...,2N_m$), the elements of

$$\mathbf{u}=[u_1,\ldots,u_{2N_m}]^T \tag{15}$$

which are specified by a control law. The maglev vehicle is subject to guideway deviation, $\mathbf{w}$, which is the superposition of the guideway deflection, $\mathbf{w}_s$, (from the guideway model of Section 2.3) and the guideway irregularity, $\mathbf{w}_d$, due to random manufacturing and construction practice, settlement, etc. The state variables include the trim current, $\mathbf{i}$, and the vehicle state, $\mathbf{x}_v$,

$$\mathbf{i}=[i_1,\ldots,i_{2N_m}]^T,\ \mathbf{x}_v=[y_c,z_c,\phi_c,\theta_c,\psi_c,\dot{y}_c,\dot{z}_c,\omega_x,\omega_y,\omega_z]^T \tag{16),(17}$$

where i_j ($j=1,...,2N_m$) is solved from Eq. (13), and $\mathbf{x}_v$ is the solution of the vehicle equations of motion (1)-(8). The output is the air gap vector, $\mathbf{h}$,

$$\mathbf{h}=[h_1,\ldots,h_{2N_m}]^T \tag{18}$$

where h_j ($j=1,...,2N_m$) is the air gap at module j. The feedback and feedforward controllers shown in Fig. 3 are described in the following section.

3 PREVIEW CONTROL SCHEME

3.1 Plant Linearization

The nonlinear plant model, consisting of the vehicle and magnet modules, is linearized such that a control law can be designed. The linearization is about the nominal point where all plant state variables are set to zero and the air gap at each magnet module is equal to the nominal air gap, h_0. Detailed derivations are given in (Wang, 1995) and the final results are summarized here.

The linearized plant model can be represented by the state and output equations

$$\dot{\mathbf{x}}_p=\mathbf{A}_p\mathbf{x}_p+\mathbf{B}_p\mathbf{u}+\mathbf{E}_p\mathbf{w},\ \mathbf{y}=\mathbf{C}_p\mathbf{x}_p+\mathbf{D}_p\mathbf{w} \qquad (19),(20)$$

where the state vector, $\mathbf{x}_p$, disturbance vector, $\mathbf{w}$, control vector, $\mathbf{u}$, and output vector, $\mathbf{y}$, can be identified as

$$\mathbf{x}_p=\begin{bmatrix}\mathbf{x}\\ \mathbf{i}\end{bmatrix}=[y_c,z_c,\phi_c,\theta_c,\psi_c,\dot{y}_c,\dot{z}_c,\omega_x,\omega_y,\omega_z,i_1,\ldots,i_{2N_m}]^T \qquad (21)$$

$$\mathbf{w}=[y_{g1},\ldots,y_{g(2N_m)},z_{g1},\ldots,z_{g(2N_m)},\dot{y}_{g1},\ldots,\dot{y}_{g(2N_m)},\dot{z}_{g1},\ldots,\dot{z}_{g(2N_m)}]^T \qquad (22)$$

$$\mathbf{u}=[u_1,\ldots,u_{2N_m}]^T,\ \mathbf{y}=[h_1-h_0,\ldots,h_{2N_m}-h_0]^T \qquad (23),(24)$$

where y_{gj} and z_{gj} ($j=1,\ldots,2N_m$) are the guideway deviations observed at module j in the lateral and vertical directions, respectively. In Eqs. (19) and (20) the coefficient matrices are $\mathbf{A}_p$, $\mathbf{B}_p$, $\mathbf{C}_p$, $\mathbf{D}_p$, and $\mathbf{E}_p$, and the linear plant is a $(10+2N_m)$-th order system with $2N_m$ control inputs, $2N_m$ outputs, and $8N_m$ disturbances. With this model, the behavior of the open-loop system (the maglev vehicle with magnet modules without controller) can be examined through the eigenvalues of the system matrix, $\mathbf{A}_p$, and the control law can be derived based on the linearized state and output equations.

3.2 Optimal Preview Control With Integral Action

In order to eliminate non-zero steady-state gap errors due to constant disturbances, the linear plant is augmented by adding integrators at its outputs. The integrator dynamics are then

$$\mathbf{y}=\dot{\mathbf{y}}_I=\mathbf{C}_p\mathbf{x}_p+\mathbf{D}_p\mathbf{w} \qquad (25)$$

where $\mathbf{y}_I$ is the integrator state vector. The augmented system dynamics are represented by the combination of the plant dynamics (19)-(20) and the integrator dynamics (25), and can be written as

$$\dot{\mathbf{x}}=\mathbf{A}\mathbf{x}+\mathbf{B}\mathbf{u}+\mathbf{E}\mathbf{w},\ \mathbf{y}=\mathbf{C}\mathbf{x}+\mathbf{D}\mathbf{w} \qquad (26),(27)$$

where

$$\mathbf{A}=\begin{bmatrix}\mathbf{A}_p & \mathbf{O}\\ \mathbf{C}_p & \mathbf{O}\end{bmatrix},\ \mathbf{B}=\begin{bmatrix}\mathbf{B}_p\\ \mathbf{O}\end{bmatrix},\ \mathbf{C}=\begin{bmatrix}\mathbf{C}_p & \mathbf{O}\end{bmatrix},\ \mathbf{D}=\mathbf{D}_p,\ \mathbf{E}=\begin{bmatrix}\mathbf{E}_p\\ \mathbf{D}_p\end{bmatrix},\ \mathbf{x}=\begin{bmatrix}\mathbf{x}_p\\ \mathbf{y}_I\end{bmatrix} \qquad (28)\text{-}(33)$$

The augmented system is controlled using LQ optimal preview control. The control law can be expressed as (Hać, 1992)

$$\mathbf{u}(t)=-\mathbf{K}_c\mathbf{x}(t)-\mathbf{R}^{-1}\mathbf{B}^T\mathbf{r}(t) \qquad (34)$$

where

$$\mathbf{K}_c=\mathbf{R}^{-1}\mathbf{B}^T\mathbf{P},\ \mathbf{PA}+\mathbf{A}^T\mathbf{P}-\mathbf{PBR}^{-1}\mathbf{B}^T\mathbf{P}+\mathbf{Q}=\mathbf{O} \qquad (35),(36)$$

$$\mathbf{r}(t)=\int_0^{t_p}e^{(\mathbf{A}-\mathbf{BR}^{-1}\mathbf{B}^T\mathbf{P})^T\sigma}\mathbf{PE}\mathbf{w}(t+\sigma)d\sigma \qquad (37)$$

where t_p is the preview time and $\mathbf{Q}$ and $\mathbf{R}$ are symmetric weighting matrices which are semi-positive and positive definite, respectively. From optimal control theory, it can be shown that the optimal control, $\mathbf{u}(t)$, exists and the resulting closed-loop system is asymptotically stable if the system $(\mathbf{A}, \mathbf{B})$ is stabilizable and the system $(\mathbf{A}, \mathbf{H})$, where $\mathbf{H}$ is a square matrix with $\mathbf{H}^T\mathbf{H}=\mathbf{Q}$, is detectable (Hać, 1992).

The control law (34) consists of a feedback part (first term) and a feedforward part (second term). The optimal feedback gain matrix, $\mathbf{K}_c$, in the feedback part is the same as the one used in linear quadratic regulator (LQR) problems. Consequently, many linear quadratic (LQ) design methods developed in the literature can be applied to select the weighting matrices and shape the required system response. The input to the feedforward part is the preview information, $\mathbf{w}(t+\sigma)$ for $\sigma\in[0,t_p]$. If no preview information is available, the controller consists solely of the feedback controller.

3.3 Control System Design

The weighting matrices $\mathbf{Q}$ and $\mathbf{R}$ are two controller design parameters chosen to meet the required performance specifications, such as appropriate bandwidth and relative stability, and limits on key state and control variables. In this work, a conventional method of selecting $\mathbf{Q}$ and $\mathbf{R}$ suggested by Bryson and Ho (1969) is adopted:

$$\mathbf{Q}=\mathrm{diag}\left(y_{\max}^{-2},z_{\max}^{-2},\phi_{\max}^{-2},\theta_{\max}^{-2},\psi_{\max}^{-2},\dot{y}_{\max}^{-2},\dot{z}_{\max}^{-2},\omega_{x,\max}^{-2},\omega_{y,\max}^{-2},\omega_{z,\max}^{-2},i_{1,\max}^{-2},\ldots,i_{2N_m,\max}^{-2},y_{I1,\max}^{-2},\ldots,y_{I(2N_m),\max}^{-2}\right) \qquad (38)$$

$$\mathbf{R}=\mathrm{diag}\left(u_{1,\max}^{-2},\ldots,u_{2N_m,\max}^{-2}\right) \qquad (39)$$

Using the maglev system parameters (representative of the Grumman National Maglev Initiative design) listed in Table 1, the following constraints are selected. The limit on the lateral and vertical CG displacements is chosen as $y_{\max}=z_{\max}=0.01$m, which is of the same order of magnitude as the allowed gap variation (*i.e.*, ±10 mm maximum gap error with 40 mm nominal gap). The limit on the roll, pitch, and yaw displacements is taken as $\phi_{\max}=\theta_{\max}=\psi_{\max}=0.01$rad (0.57°) to reflect the physical constraints on these displacements. A maximum current of 300 A is used for the estimated limit on the trim currents, $i_{j,\max}$ ($j=1,\ldots,2N_m$). Since a unity D.C. gain is desired for the magnet modules, the limit on the voltages, $u_{j,\max}$ ($j=1,\ldots,2N_m$), is chosen as 300V

Table 1: Parameters of Maglev Model

Parameter	Symbol	Value	Unit
vehicle mass	M_v	30,600	kg
vehicle length	L_v	18	m
vehicle height	h_v	3.9	m
vehicle width	w_v	3.8	m
nominal air gap	h_0	0.04	m
height, magnet centroid to vehicle CG	h_c	1.09	m
width, magnet centroid to vehicle CG	w_c	0.76	m
roll moment of inertia	I_x	7.4×10^4	kg-m^2
pitch moment of inertia	I_y	8.0×10^5	kg-m^2
yaw moment of inertia	I_z	9.6×10^5	kg-m^2
magnet cant angle	β	35	deg
number of modules on each side	N_m	2	None
number of magnets in each module	n_m	12	None
number of turns in SC coil	N_{SC}	1020	None
number of turns in normal coils	N_n	96	None
face area of each magnetic pole	A_m	0.04	m
total resistance of normal coils	R_c	1.0	ohm
permeability of air	μ_0	$4\pi\times10^{-7}$	weber/A-m
span length	L_s	21.3	m
span mass per unit length	γ	4777	kg-m^2
bending rigidity	EI	1.84×10^{10}	N-m^2
first-mode span damping ratio	ζ	0.03	None

which corresponds to a steady-state trim current of 300A. The weightings on the CG velocities affect the speed of vehicle response, and they can be adjusted to achieve desired damping ratios and natural frequencies. These weightings are initially selected as $\dot{y}_{max} = \dot{z}_{max} = 1$ m/s and $\omega_{x,max} = \omega_{y,max} = \omega_{z,max} = 1$ rad/s. The speed of integral action is dominated by the weightings on the integrator state variables where an estimated limit of $y_{Ij,max}$=0.001 m-s (j=1,...,$2N_m$) is initially selected. It should be noted that the translation of specifications into the selection of **Q** and **R** matrices is not straightforward nor unique, and often adjustments are needed. The controller design is an iterative process.

The properties of the open-loop system can be examined by calculating the eigenvalues of the linearized plant model. The eigenvalues and the corresponding damping ratios and natural frequencies are summarized in Table 2. The first ten eigenvalues characterize the carbody motion without feedback control. The remaining eigenvalues are the inverses of the magnet time constants. As shown in Table 2, the natural frequencies of the magnet eigenvalues ($\lambda_{o,11}$,...,$\lambda_{o,14}$) are much larger than the natural frequencies of the carbody eigenvalues ($\lambda_{o,1}$,...,$\lambda_{o,10}$) indicating a faster dynamic response for the magnets than for the carbody. (This difference can be increased further by adding resistance to the normal coil.) The three eigenvalues located in the right half-plane indicate that the open-loop system is unstable.

The closed-loop system can be obtained by applying the feedback control law (34) to the augmented state equation (26). The eigenvalues of the closed-loop system matrix and the corresponding damping ratios and natural frequencies are reported in Table 3. The first ten eigenvalues are the vehicle modes which are all located in the left half-plane. The unstable modes in the open-loop system have been shifted into the stable region. Also, the damping ratios of the very lightly damped modes, $\lambda_{o,1}$ and $\lambda_{o,2}$, are increased from 0.00851 to an acceptable value of 0.25 ($\lambda_{c,1}$ and $\lambda_{c,2}$), with the natural frequency almost unchanged. Other carbody modes are well damped with damping ratios greater than 0.5. For efficient use of the control effort, the carbody modes have been placed at approximately uniform distances from the origin, ranging from 15.1 to 25.2 rad/s. The integral action inserts four additional eigenvalues in the closed-loop system, represented by the eigenvalues from $\lambda_{c,11}$ through $\lambda_{c,14}$. The last four eigenvalues in Table 3 are the SC magnet modes which have larger natural frequencies, compared to the uncontrolled situation, implying faster magnet dynamics.

Table 2: Eigenvalues of Open-Loop System

Symbol	Eigenvalue	Damping Ratio	Natural Freq. (rad/s)
$\lambda_{o,1}$ & $\lambda_{o,2}$	$-0.158 \pm j18.5$	0.00851	18.5
$\lambda_{o,3}$ & $\lambda_{o,4}$	$-0.370 \pm j1.49$	0.241	1.5
$\lambda_{o,5}$	−11.7	1.0	11.7
$\lambda_{o,6}$	−16.4	1.0	16.4
$\lambda_{o,7}$	−18.8	1.0	18.8
$\lambda_{o,8}$	16.4	−1.0	16.4
$\lambda_{o,9}$	14.5	−1.0	14.5
$\lambda_{o,10}$	10.9	−1.0	10.9
$\lambda_{o,11}$	−170.3	1.0	170.3
$\lambda_{o,12}$	−170.9	1.0	170.9
$\lambda_{o,13}$	−171.6	1.0	171.6
$\lambda_{o,14}$	−172.0	1.0	172.0

Table 3: Eigenvalues of Closed-Loop System

Symbol	Eigenvalue	Damping Ratio	Natural Freq. (rad/s)
$\lambda_{c,1}$ & $\lambda_{c,2}$	$-4.31 \pm j16.6$	0.250	17.2
$\lambda_{c,3}$ & $\lambda_{c,4}$	$-7.65 \pm j13.0$	0.508	15.1
$\lambda_{c,5}$ & $\lambda_{c,6}$	$-12.2 \pm j13.9$	0.659	18.5
$\lambda_{c,7}$ & $\lambda_{c,8}$	$-13.1 \pm j13.3$	0.701	18.7
$\lambda_{c,9}$ & $\lambda_{c,10}$	$-20.3 \pm j15.0$	0.804	25.2
$\lambda_{c,11}$	−10.7	1.0	10.7
$\lambda_{c,12}$	−14.4	1.0	14.4
$\lambda_{c,13}$	−16.6	1.0	16.6
$\lambda_{c,14}$	−23.8	1.0	23.8
$\lambda_{c,15}$	−242.5	1.0	242.5
$\lambda_{c,16}$	−242.9	1.0	242.9
$\lambda_{c,17}$	−243.4	1.0	243.4
$\lambda_{c,18}$	−243.7	1.0	243.7

4 MAGLEV SYSTEM PERFORMANCE

4.1 Simulation Model

The complete nonlinear maglev system, consisting of models of the vehicle, guideway, magnets, and feedback and feedforward controllers, is represented by the block diagram of Fig. 3. The inputs to the overall system are $\mathbf{w}_d(t)$, due to guideway irregularity and $\mathbf{w}(t+\sigma)$, representing the preview information in front of the vehicle. The outputs of the system are the air gap, $\mathbf{h}(t)$, and the vehicle state, $\mathbf{x}_v(t)$.

Guideway irregularities occur as a result of construction tolerances and environmental conditions. In this work, the guideway irregularity profile described in (Snyder and Wormley, 1977) is adopted. It can be represented as the summation of the following effects: (*i*) surface roughness of the guideway iron rails, (*ii*) span vertical offsets due to misalignments of the guideway spans, (*iii*) column height variations, and (*iv*) intentionally imposed camber of the guideway spans to compensate for vehicle loading. Since these irregularities result from a wide variety of effects, it is assumed that the amplitudes of each type of irregularity (except for the surface roughness) are normally distributed random numbers. With prescribed mean values and standard deviations, the guideway irregularities may represent the tolerance requirements of the guideway structure. Figure 4 shows a combined guideway irregularity in the lateral and vertical directions, where the guideway roughness is in the normal direction of the rail face while the guideway steps, ramps, and cambers are in the vertical direction. The surface roughness is modeled by the power spectral density function (PSD) of the form: $\Phi(\Omega)=A_r/\Omega^2$, where A_r is a roughness parameter (Katz, *et al.*, 1974). Here, $A_r=6.1\times10^{-8}$ m, representing a high quality welded rail (Wormley, *et al.*, 1992). The step deviation, column height, and camber amplitude for each span are generated randomly with a zero mean and a 2 mm standard deviation.

The dynamics of the complete maglev system are described by the combination of the dynamic equations of each subsystem: (*i*) ten first-order ODEs for the vehicle model, (*ii*) $2N_m$ first-order ODEs for the magnet modules, (*iii*) $2N_m$ first-order ODEs for the integrator dynamics in the feedback controller, and (*iv*) $2n_s$ second-order ODEs for the guideway flexibility for each of the two consecutive spans. The total number of state variables is $10 + 4(N_m + n_s)$. For a vehicle with four magnet modules (two per side) and a guideway modeled with three modes per span, thirty state variables are needed to characterize the complete system. In the simulation model, it is assumed that the vehicle state, $\mathbf{x}_v(t)$, the trim current, $\mathbf{i}(t)$, and the air gap, $\mathbf{h}(t)$, can be measured perfectly, and that the preview vector, $\mathbf{w}(t+\sigma)$, is available *a priori*.

4.2 Performance Studies

In the simulation studies, the maglev vehicle operates over a multi-span elevated guideway at constant speed. Objectives of the maglev system are to: (*i*) maintain each magnet module/iron rail air gap within a safe margin to prevent vehicle/guideway contact, (*ii*) ensure that the control voltages are within feasible limits, and (*iii*) attain maximum ride comfort. To meet these objectives, the following safety- , energy- and comfort-related performance measures are posited.

The allowed air gap is chosen to be between 30 mm and 50 mm. The smallest acceptable gap of 30 mm precludes vehicle/guideway contact while assuring a reasonable safety margin. Gap deviation from the nominal value of 40 mm is viewed as a safety-related performance measure. The required control voltages are constrained within ±300 V to prevent saturation of the magnetic forces. The control voltage is used as an indication of energy cost. The ride comfort is measured by comparing carbody accelerations at the car front and rear to the ISO ride quality criteria (ISO, 1978). The ISO ride quality criteria specify limits on root mean square (RMS) lateral and vertical accelerations in one-third octave bands over a specified range of frequencies.

To illustrate the combined influence of guideway irregularities and deflections upon vehicle performance, the maglev vehicle was tested at 500 kph on a 4-span flexible guideway with guideway roughness and step, ramp, and camber geometry errors. Four magnet modules (two on each side) are assumed for the vehicle.

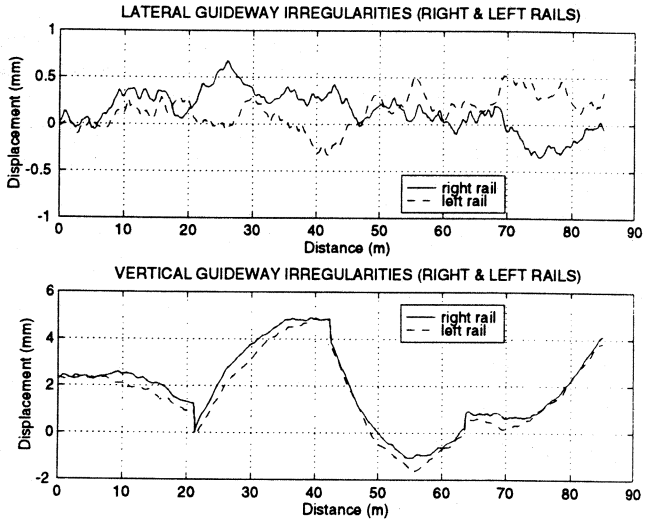

Figure 4 Combined Guideway Irregularities

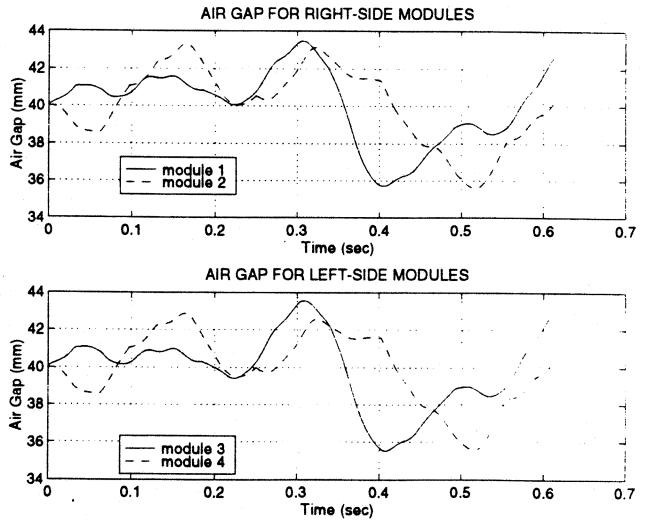

Figure 5 Air Gaps at 500 kph

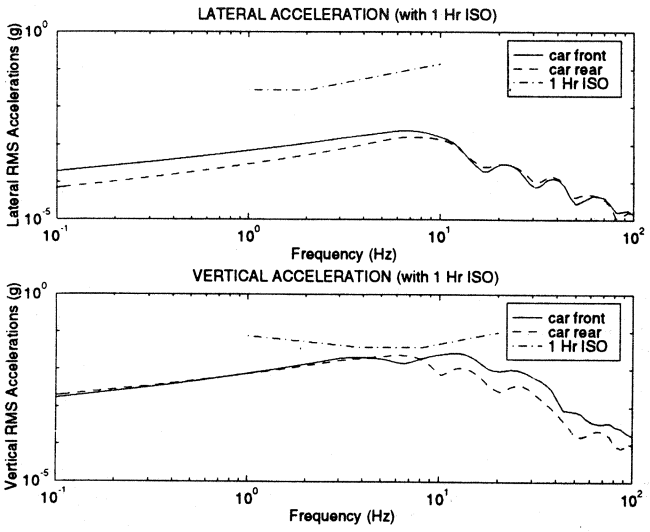

Figure 6 RMS Accelerations at 500 kph

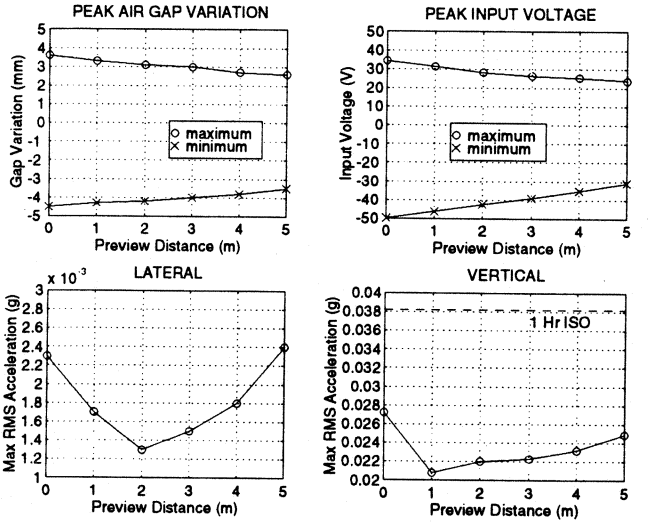

Figure 7 System Performance with Preview at 500 kph

The simulation studies were performed assuming the guideway profile depicted in Fig. 4. With this profile and no feedforward (preview) control, the time histories of the air gap variation shown in Fig. 5 are predicted. The corresponding frequency responses for the RMS accelerations in the lateral and vertical directions are shown in Fig. 6. The results demonstrate that (*i*) the air gap deviations are within the safety margin (the maximum deviation being 4.5 mm), and (*ii*) both the lateral and vertical acceleration levels are below the ISO one-hour limit. The voltage time history results (not shown here) also indicate compliance well within the feasibility limits, and, thus, the zero preview case meets the performance specifications.

To explore the potential for improved vehicle performance, the effects of preview control were studied. The results are summarized in Fig. 7 which displays the peak values of the air gap, input voltage, and RMS accelerations for different preview distances, where the preview distance is the product of preview time and vehicle speed. The baseline case of zero preview distance (from the simulation study of Figs. 5 and 6) has the highest values of gap error, voltage, and vertical RMS acceleration. As the preview distance increases, the peak air gap variation and input voltage decrease. For example, with a 5 m preview distance, the peak voltage (–31.0 V) is 62.2% of the baseline case without preview (–49.8 V). For all cases tested, the performance measures are well below their specifications. Figure 7 also shows that the vertical peak RMS acceleration exhibits a minimum at 1 m preview distance. Increasing preview distance tends to raise the acceleration but reduce the gap error. Thus, there is a trade-off between the gap error and carbody acceleration. In summary, although preview control offers a potential performance improvement in terms of reducing the gap error and the magnet input voltage, there appears to be a characteristic preview distance that minimizes the carbody acceleration.

5 CONCLUSION

A control law based on optimal preview control with integral action is proposed for the combined lift and guidance system of an EMS maglev vehicle. The effectiveness of the control approach is examined using a comprehensive model that includes the vehicle dynamics in the lateral, vertical, roll, pitch, and yaw directions, the magnet dynamics, and the effects of guideway flexibility and irregularity.

Simulation testing reveals that preview control can be effective in reducing the input voltages and gap errors. Although these measures decrease as the preview distance increases, the vehicle performance is limited due to a trade-off between the acceleration and gap error. There appears to be a characteristic preview distance that optimizes the maglev system performance. Further studies into the effectiveness of the proposed strategy are underway.

6 ACKNOWLEDGMENT

The work described in this paper is based in part on studies performed in support of the Volpe Center activities on the FRA sponsored High Speed Guided Ground Transportation (HSGGT) safety program. The authors are grateful to Mr. D. Tyrell and Dr. H. Weinstock (DOT's Volpe Center, Cambridge, MA), to Dr. I. Haque (Clemson University), and to engineers at Battelle (Columbus, OH) for their technical contributions.

7 REFERENCES

Anderson, B.D.O. and Moore, J.B., 1990, *Optimal Control: Linear Quadratic Methods*, Prentice Hall Inc., Englewood Cliffs, New Jersey.

Bender, E.K., 1968, "Optimum Linear Preview Control With Application to Vehicle Suspension," *Journal of Basic Engineering, Transactions of the ASME*, Vol. 90, No. 2, pp. 213-221.

Bryson, A.E. and Ho, Y., 1969, *Applied Optimal Control: Optimization, Estimation, and Control*, Blaisdell Publishing Company, Waltham, Massachusetts.

Cherchas, D.B., 1979, "A Dynamics Simulation for a High Speed Magnetically Levitated Guided Ground Vehicle," *Journal of Dynamic Systems, Measurement and Control*, Vol. 101, pp. 223-229.

Haĉ, A., 1992, "Optimal Linear Preview Control of Active Vehicle Suspension," *Vehicle System Dynamics*, Vol. 21, pp. 167-195.

Heinrich, K. and Kretzschmar, R. eds., 1989, *Transrapid Maglev System*, Hestra-Verlag, Dramstadt.

Iskander, M.F., 1992, *Electromagnetic Fields and Waves*, Prentice-Hall Inc., Englewood Cliffs, New Jersey.

ISO, 1978, "Guide for the Evaluation of Human Exposure to Whole-Body Vibration," *ISO Standard 2631*, International Organization for Standardization.

Katz, R.M., Nene, V.D., Ravera, R.J., and Skalski, C.A., 1974, "Performance of Magnetic Suspensions for High Speed Vehicles Operating Over Flexible Guideways," *Journal of Dynamic Systems, Measurement and Control*, June, pp. 204-212.

Kortüm, W. and Utzt, A., 1984, "Control Law Design and Dynamic Evaluations for a Maglev Vehicle With a Combined Lift and Guidance Suspension System," *Journal of Dynamic Systems, Measurement and Control*, Vol. 106, pp. 286-292.

Langlois, R.G. and Anderson, R.J., 1995, "Preview Control Algorithms for the Active Suspension of an Off-Road Vehicle," *Vehicle System Dynamics*, Vol. 24, pp. 65-97.

Louam, N., Wilson, D.A., and Sharp, R.S., 1992, "Optimization and Performance Enhancement of Active Suspensions for Automobiles under Preview of the Road," *Vehicle System Dynamics*, Vol. 21, pp. 39-63.

Peng, H. and Tomizuka, M., 1993, "Preview Control for Vehicle Lateral Guidance in Highway Automation," *Journal of Dynamic Systems, Measurement and Control*, Vol. 115, pp. 679-686.

Proise, M., Deutsch, L., Gran, R., Herbermann, R., Kalsi, S., and Shaw, P., 1993, "System Concept Definition of the Grumman Superconducting Electromagnetic Suspension (EMS) Maglev Design," *Maglev 93 Conference*, Argonne National Laboratory, May 19-21, Paper No. OS4-4.

Snyder, J.E. and Wormley, D.N., 1977, "Dynamic Interactions Between Vehicles and Elevated, Flexible Randomly Irregular Guideways," *Journal of Dynamic Systems, Measurement and Control*, March, pp. 23-33.

Tomizuka, M., 1976, "Optimal Linear Preview Control With Application to Vehicle Suspension – Revisited," *Journal of Dynamic systems, Measurement and Control*, Vol. 98, No. 3, pp. 309-315.

Wang, S.K., 1995, "Levitation and Guidance of a Maglev Vehicle Using Optimal Preview Control," *Doctoral Dissertation*, Department of Mechanical Engineering, Carnegie Mellon University, May.

Wormley, D.N., Thornton, R.D., Yu, S.-H., and Cheng, S., 1992, "Interactions Between Magnetically Levitated Vehicles and Elevated Guideway Structures," U.S. Department of Transportation Technical Report DOT/FRA/NMI-92/23.